Tapered foils favor traveling-wave kinematics to enhance the performance of flapping propulsion

Pierre Leroy-Calatayud [1], Matteo Pezzulla [1,*] Armelle Keiser,[1,2,†]
Karen Mulleners [2] and Pedro M. Reis [1,‡]

[1]*Flexible Structures Laboratory, Institute of Mechanical Engineering, École Polytechnique Fédérale de Lausanne (EPFL), 1015 Lausanne, Switzerland*
[2]*Unsteady Flow Diagnostics Laboratory, Institute of Mechanical Engineering, École Polytechnique Fédérale de Lausanne (EPFL), 1015 Lausanne, Switzerland*

We report results from an experimental investigation on the fluid-structure interactions of *flapping foils* with tapered thickness profiles actuated in a quiescent viscous fluid. We seek to assess the propulsive performance of two sets of flapping foils; one with a fixed average bending stiffness, the other one with a fixed mass ratio. We find that foils that are stiffer towards the root than at their tip produce higher values of thrust and efficiency simultaneously, over a wide range of driving frequencies. Our kinematic analysis reveals that more tapered foils naturally develop a traveling-wave-dominated motion. We perform particle image velocimetry to relate the dynamics and kinematics of the flapping foils to the dynamics of the surrounding fluid. For more tapered foils, we observe a stronger vorticity production and a wake pattern with enhanced downstream speed of the fluid. Our paper provides experimental evidence that tapered stiffness distributions robustly enhances propulsive performance.

I. INTRODUCTION

Flying insects and many aquatic animals rely on flapping appendages for locomotion [1–3]. Motivated by flexibility, a common feature to both fish fins [4] and insect wings [5], theoretical [6–10], computational [11–14], and experimental studies [8–10,15–18] have focused on the dynamics of flexible platelike structures heaving or pitching passively in a fluid. The ability to deform in response to fluid loading tends to increase the performance compared to equivalent rigid systems both in terms of thrust production and efficiency. It has been proposed that the resonant behavior arising due to the coupled fluid-structure interaction (FSI) is at the origin of this enhancement [19,20].

The majority of past studies have focused on propulsors with a uniform bending stiffness. However, the mechanical properties of wings [21] and fins [22] often change along their span or chord. Despite the relevance to the original biological systems, this more general case of a spatially varying (heterogeneous) bending stiffness has only recently started to attract attention. Computational and experimental results suggest that structures with a stiffer leading edge are more efficient than those with an equivalent uniform stiffness [23–27]. A contrasting claim that propulsors with their flexibility concentrated at the root perform better has also been reported [28,29]. In both cases, it

---

*Current address: Department of Mechanical and Production Engineering, Slender Structures Laboratory, Århus University, Inge Lehmanns Gade 10, 8000 Århus C, Denmark.

†Current address: Grenoble Alpes University, CEA, LETI, DTBS, LSMB, 38000 Grenoble, France.

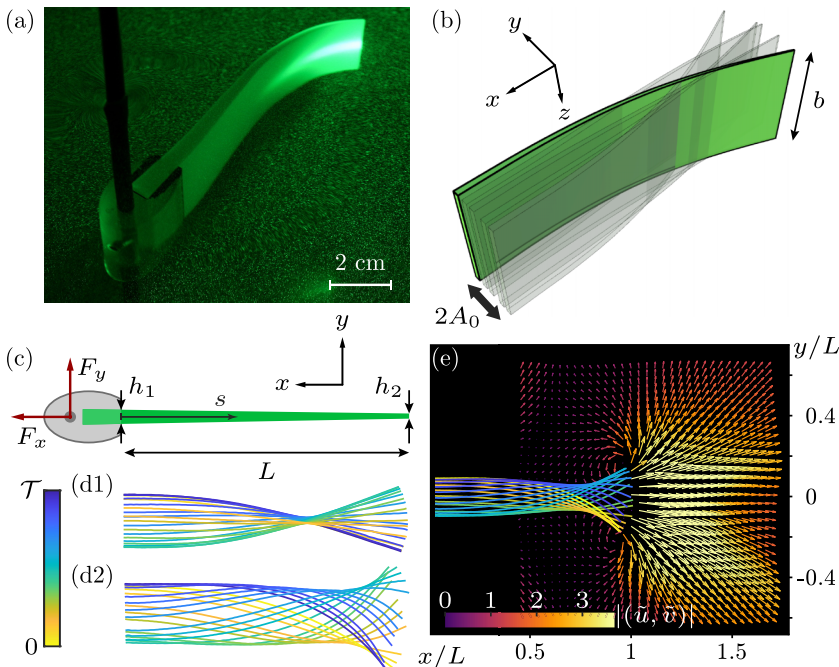‡Corresponding author: pedro.reis@epfl.ch

FIG. 1. (a) Photograph and (b) schematic of a flexible tapered flapping foil, heaving with amplitude A_0 along the y axis. (c) Schematic of the flapping foil and reaction forces F_x and F_y measured at the clamp. (d) Center-line deformation for a flat specimen ($\alpha = 0$) (d1) and a highly tapered one ($\alpha = 0.90$) (d2), actuated at three times their respective resonant frequency, $f = 3f_0$. (e) Period-averaged velocity field of the surrounding fluid measured with particle image velocimetry (PIV). The bending profiles measurements and the PIV were performed separately (flapping foil $\alpha = 0.90$ at $f = 2f_0$).

seems that distributing the stiffness is an asset in flapping propulsion, yet the physical mechanisms at the core of this enhancement remain unclear. A recent computational study performed a systematic parametric investigation of a two-dimensional (2D) inviscid system and emphasized the importance of fixing the mean stiffness when studying heterogeneous bending stiffnesses [30]. This feature has been rarely considered previously. To gain physical insight into the mechanisms at the core of the propulsion improvements observed in tapered flexible systems, there is a need for controlled experiments and high-precision data sets that independently target the effects of the overall stiffness and its distribution.

Here, we investigate the kinematics and dynamics of tapered elastomeric flapping propulsors, hereon referred to as *flapping foils*, subjected to a heaving motion in a quiescent viscous fluid [Fig. 1(a)]. Our fabrication procedure allows for the manufacturing of flapping foils with precise control over their geometric and physical properties. For example, we can fix the average bending stiffness whereas exploring different tapering ratios. A harmonic heaving motion is imposed at the root of the flapping foil [Fig. 1(b)], and we quantify the resulting reaction forces and deformation profiles [Fig. 1(c)]. Our goal is to evaluate the effect of thickness tapering on the hydrodynamic performance of the foils. First, we will quantify the thrust coefficient and efficiency, finding that both quantities increase significantly for foils that are stiffer at the root. Then, we analyze the deformation profiles [Fig. 1(d)] to connect this higher efficiency to traveling-wave kinematics. Finally, we will turn our attention to the fluid [Fig. 1(e)] and perform particle image velocimetry (PIV) to relate the performance enhancement to the structure of the generated wake flow. We find that better performing flapping foils are associated with a stronger vorticity and a downstream-favored orientation of the produced flow.

II. EXPERIMENTS

A. Description of the flapping-foil samples

In Fig. 1, we present photographs and schematics of our experimental flapping foils. The geometry of the foils was inspired by the computational work of Yeh *et al.* [26]. The length, $L = 95.0$ and width, $b = 37.5$ mm are fixed for all specimens, setting the aspect ratio $L/b = 2.5$. The thickness $h(s)$ decreases linearly along the arc-length $s \in [0, L]$ with the values of $h_1 > h_2$ at the root and the tip, respectively. The *tapering ratio* is defined as $\alpha = 1 - h_2/h_1$.

We introduce two sets of six flapping foils, which we refer to as: (i) iso-$\langle B \rangle$ and (ii) iso-M:

(i) The iso-$\langle B \rangle$ foils are characterized by a fixed value of mean bending stiffness $\langle B \rangle := (\int_0^L B \, ds)/L$. The tapering ratio α is systematically varied with six pairs of h_1, $h_2 \in [0.6, 6.2]$ mm. The values of the tapering ratio lie in the range from $\alpha = 0$ (a flat sample) to $\alpha = 0.90$ (a highly tapered one). For a linear thickness profile $h(s) = h_1(1 - \alpha s/L)$, the mean bending stiffness is $\langle B \rangle = B_1[1 - (\alpha^3 - 4\alpha^2 + 6\alpha)/4]$, where B_1 is the bending stiffness at the root. The mass ratio $M = \langle \rho_s h \rangle/(\rho_f L)$ as defined in Ref. [30] of this set varies in the range of $0.041 \leqslant M \leqslant 0.053$.

(ii) The iso-M foils have a fixed value of the mass ratio $M = \langle \rho_s h \rangle/(\rho_f L) = 0.052 \pm 0.001$, where ρ_s and ρ_f are the densities of the structure (foil) and the surrounding fluid, respectively. The average bending stiffness of this set of iso-M foils varies in the range $\langle B \rangle \in [0.21, 0.34] \times 10^{-3}$ N m^2. (The details on the measurements of $\langle B \rangle$ are provided below.)

For both sets, a fix value of $\langle B \rangle$, (respectively, M) is chosen, as well as the set of values for α. The thicknesses h_1 and h_2 are computed to meet both requirements. The rationale for introducing these two distinct sets of foils (iso-$\langle B \rangle$ and iso-M) lies in the fact that it is not possible to simultaneously fix both M and $\langle B \rangle$ whereas keeping the same geometry and using a homogeneous material. On the one hand, inspired by Ref. [30], we want to investigate samples with a fixed mean bending stiffness $\langle B \rangle$. On the other hand, a varying mass ratio, M, indicates a change in the balance of hydrodynamic and elastic forces at play. Indeed, M can be used as a distinguishing feature between insect wings and fish fins. Fish fins are naturally buoyant and have a density ratio of $\rho_f/\rho_s \sim 1$. Insect wings are made of organic materials that are much denser than air and have a density ratio of $\rho_f/\rho_s \ll 1$. Hence, M tends to be substantially higher for fliers than for swimmers and can affect the overall behavior of the system significantly [19]. For both sets, the mass ratio M is relatively low and falls within the regime relevant for fish.

B. Fabrication of the samples

Our flapping foils are fabricated by pouring an elastomeric solution [vinyl polysiloxane, (VPS), Elite Double 32, Zhermack] into a mold assembly of laser-cut acrylic pieces. Figure 2(a) presents a photograph and a schematic of the molds, containing a central triangular spacer that is cut to the desired linear thickness profile. After curing of the VPS polymer, the flapping foils are preconditioned by immersing them in silicone oil (Bluesil 47 V 10, Silitech AG, density $\rho_f = 950$ kg/m^3, dynamic viscosity $\mu = 0.0105$ Pa s, at $23\,^\circ$C); the same fluid used for the subsequent experiments.

The silicone bath causes the foils to undergo isotropic volumetric swelling [31] $V = \lambda^3 V_{dry}$ (V_{dry} is the initial volume) with a linear swelling coefficient $\lambda = 1.25$, determined by measuring the increased length and width of a reference foil after they reach a steady value [32]. The thickness profile $h(s)$ of the foils is measured using digital image analysis both before and after swelling.

C. Bending stiffness of the samples

To characterize the bending stiffness of the foils, we perform a cantilever test by clamping each oil-swollen sample at its root and loading it under gravity. The deformed profiles are extracted through image processing and fitted through a boundary value problem solver to an Euler's
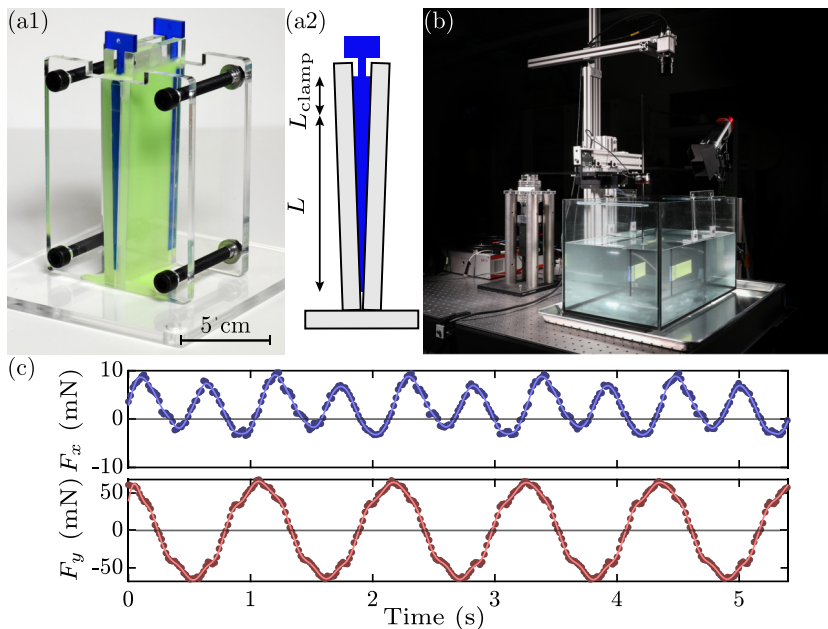
FIG. 2. Fabrication, experimental setup, and force measurements. (a1) and (a2) Photograph and schematic of the mold used to fabricate the flapping foils. (b) Experimental apparatus. (c) Time series of propulsive force F_x (top) and the driving force F_y (bottom) as raw (dots) and low-passed (line) signals for $\alpha = 0.54$, $\tilde{f} = 1$.

elastica [33], including the tapered thickness,

$$(1 - \alpha\bar{s})^3\theta'' - 3\alpha(1 - \alpha\bar{s})^2\theta' + \frac{1}{\beta}\left[\frac{\alpha}{2}(1 - \bar{s}^2) - (1 - \bar{s})\right]\cos\theta = 0, \tag{1}$$

where $\bar{s} = s/L \in [0, 1]$ is the nondimensional arc length along the foil, $(\cdot)'$ denotes differentiation with respect to $\bar{s}$, and $\theta(\bar{s})$ is the local angle of the tangent to the undeformed centerline. The dimensionless parameter $\beta = B_1/(\rho_s g b h_1 L^3)$ represents the balance between the elastic and the gravitational forces, where g is the gravitational acceleration, $\rho_s = 1062 \text{ kg/m}^3$ is the density of the swollen VPS, and B_1 is the bending stiffness at the root of the flapping foil.

The cantilever test yields a direct measure of B_1 after which we determine a mean stiffness $\langle B \rangle = (0.19 \pm 0.02) \times 10^{-3} \text{ N m}^2$ for all six flapping foils of the iso-$\langle B \rangle$ set and $\langle B \rangle \in [0.21, 0.34] \times 10^{-3} \text{ N m}^2$ for the iso-M set.

D. Experimental apparatus

A photograph of the experimental apparatus is shown in Fig. 2(b). The fluid tank $(50 \times 30 \times 30 \text{ cm}^3)$ is filled with the silicone oil to a height of 18 cm. The tapered flapping foil is mounted to the driving mechanism by a three-dimensional-printed clamp (Clear Resin, Formlabs) at the center of the tank. The shape of the internal slit of the clamp is customized depending on the geometry of the tapered foil to ensure a snug fit, whereas the external shape is the same for all clamps [see Fig. 1(a)]. The clamp is connected through a vertical carbon-fiber rod to the driving mechanism. This mechanism comprises a slider-crank system connected to a stepper motor through an air bearing, producing a linear harmonic (heaving) motion $A(t) = A_0\cos(2\pi f t)$ at the clamp, where t and f denote time and frequency, respectively, with an amplitude $A_0 \approx 0.09L$ (similar to Ref. [26] with $A_0 = 0.1L$). A six-axis force/torque sensor (Mini40 SI-20-1, ATI Industrial Automation) connects the driving mechanism to the carbon rod holding the flapping foil, enabling measurements of the reaction forces at the clamp. The nominal resolution of the force sensor, as

stated by the manufacturer, is 5 mN but with appropriate averaging and filtering we can reach 1-mN resolution. In Fig. 2(c), we present representative examples of the time series of the measured reaction forces F_x and F_y. We note a slight asymmetry in the F_x signal, which can be due to slight imperfections of the setup or variations in the clamping procedure. To reduce the influence of the asymmetry of individual time series on the time-averaged quantities, we re-installed the foils each time before repeating experiments for a given parameter configuration. Simultaneously, a scientific camera (Flea3, Flir Systems) placed above the tank captures the deformation profiles of the flapping foils. The motor, the force sensor, and the camera, are all synchronized and computer controlled.

E. Dynamical properties of the flapping foils

Above, we characterized the geometry (from image processing) and bending stiffness (from cantilever tests) of the flapping foils. Now, with the full apparatus, we turn to the dynamical properties. We start by measuring the first resonant frequency f_0 of the flexural motion of each foil in the fluid. After abruptly stopping the oscillatory driving motion of the foil, the time series of the tip deflection is recorded, and f_0 is determined from the dominant peak in the fast Fourier transform of the decaying signal. The measured resonant frequencies of the six foils from the flat sample to the most tapered one are in the range $0.74 \leqslant f_0$ [Hz] $\leqslant 1.01$. The *frequency ratio* between the driving frequency f and the measured resonance frequency will be denoted by $\tilde{f} = f/f_0$.

III. PERFORMANCE OF THE FLAPPING FOILS: POWER, THRUST, AND EFFICIENCY

We start our experimental investigation by evaluating the hydrodynamic performance of the flapping foils by simultaneously recording time series of the reaction forces at the clamp, F_x and F_y [representative example given in Fig. 2(c)], and the full deformation profiles. The frequency ratio is systematically varied in the range $0.3 \leqslant \tilde{f} \leqslant 3.8$ in steps of 0.1 with refinement around the resonance frequency. The data are recorded over ten cycles $\mathcal{T} = 1/f$. The frequency sweep is repeated five times to quantify experimental uncertainties and reproducibility, each time re-installing the foil in the tank. In the absence of background flow, we define the Reynolds number based on the characteristic flapping frequency f [13] as $\mathrm{Re} = \rho_f(2\pi f)A_0 L/\mu$, which was varied in the range of $90 \leqslant \mathrm{Re} \leqslant 2000$.

To compare the propulsive characteristics of the different flapping foils, we will now define the thrust, C_T and power C_P coefficients by nondimensionalizing the produced thrust and input power. A measure for efficiency will follow naturally. We choose to follow the definitions proposed in Ref. [34], up to a multiplicative constant,

$$C_T = \frac{\overline{T}}{\frac{1}{2}\rho_f bL(2\pi f A_0)^2}, \quad C_P = \frac{\overline{P}}{\frac{1}{2}\rho_f bL(2\pi f A_0)^3}, \tag{2}$$

where $\overline{T} = \overline{F_x}$ is the average thrust and $\overline{P} = -\overline{v_y F_y}$ is the average power input with v_y being the lateral velocity of the root. Overlined quantities denote period averages over ten cycles. The maximum tip deflection a and the root displacement amplitude A_0 are extracted from image processing of the movies acquired simultaneously during the experiments. For each frequency sweep with a flapping foil (obtaining $\overline{P}_{\mathrm{tot}}$), we perform an additional sweep with the clamp alone (obtaining $\overline{P}_{\mathrm{clamp}}$) to then compute $\overline{P} = \overline{P}_{\mathrm{tot}} - \overline{P}_{\mathrm{clamp}}$, assuming that the clamp and the flapping foil can be treated independently. Finally, the efficiency, which we define as the ratio between thrust and input power, can be readily quantified as $\varepsilon = C_T/C_P$.

In Fig. 3(a), we plot C_T for our six iso-$\langle B \rangle$ flapping foils as a function of $\tilde{f}$, finding that the produced thrust increases with tapering ratio α. Each curve for different values of α exhibit a peak in the neighborhood of the resonant frequency $\tilde{f} = 1$. This peak is especially prominent for the lower values of α. Past resonance, the thrust produced by the flat sample drops significantly but it remains at a relatively high value for the more tapered samples. The power coefficient [Fig. 3(b)] also reaches a resonant peak but at lower frequencies ($\tilde{f} \approx 0.7$). Near resonance, samples with the
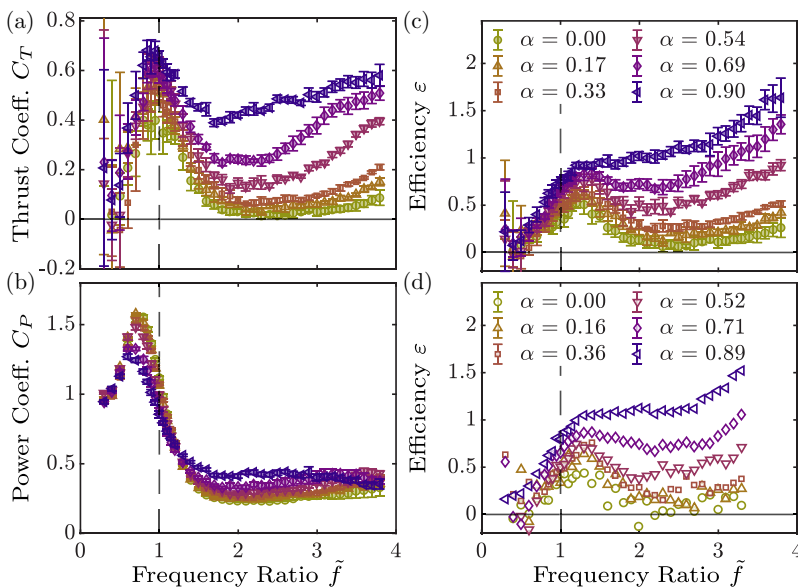
FIG. 3. Performance of the (a)–(c) iso-$\langle B \rangle$, and (d) iso-M foils as a function of the driving frequency. (a) Thrust coefficient C_T and (b) power coefficient C_P versus the driving frequency ratio $\tilde{f}$. (c) and (d) Efficiency ε as a function of $\tilde{f}$ for the (c) iso-$\langle B \rangle$ and (d) iso-M foils. The error bars in (a)–(c) correspond to the standard deviation of five runs. No error bars are included in (d) since only one run was performed for this set.

lowest values of α require the largest input power. Past resonance ($\tilde{f} > 1.3$), this trend is reversed. In Fig. 3(c), we plot the dependence of the efficiency ε on $\tilde{f}$ for the iso-$\langle B \rangle$ foils. Similar to the $C_T(\tilde{f})$ curves, the more tapered samples are more efficient across the full range of $\tilde{f}$, especially for $\tilde{f} \gtrsim 1.3$. For example, at $\tilde{f} = 2.5$, the most tapered foil ($\alpha = 0.90$) produces over 30 times more thrust and is 17 times more efficient than the flat one ($\alpha = 0$). Nearly identical behavior for $\varepsilon(\tilde{f})$ is found for the iso-M foils as shown in Fig. 3(d). In the Supplemental Material [35], we present an alternative choice for the definition of the performance coefficients yet, yielding very similar qualitative results, which conveys that our findings are robust to the exact choices of C_T and C_P. Also, additional measurements were performed for a representative iso-$\langle B \rangle$ sample close to a side wall of the tank and close to the bottom of the tank to estimate possible wall effects. In either cases, we did not observe any significant difference in the output performance.

The similarity between the results for the iso-$\langle B \rangle$ and iso-M foils indicates that α dominates their performance. The enhancement of efficiency in tapered fins was already highlighted in prior simulations [26], a finding that is corroborated by our experiments. Still, there are some quantitative differences between our results and this previous computational study. For the more tapered fins, Yeh *et al.* [26] observed lower values of C_T near resonance, compared to their flat specimen. Also, their simulations were performed at $M = 0.4$ and considered profiles with both linear thickness and linear stiffness at Re $= 250$. By contrast, our experimental system has an order of magnitude lower value of M, Re was not fixed, and the stiffness profile of our foils is cubic on s [given their linear thickness profile, $h(s) \sim s$]. As such, it is not possible to establish a direct quantitative comparison between our experimental results and the simulations in Ref. [26], even if the overall qualitative findings are similar. Here, we recall that our experimental setup operates in a quiescent fluid, a special case of flapping propulsion (*swimming*, in other words). Our main motivation for selecting these conditions was to study the fluid-structure interaction in a simplified environment. For example, this choice avoids the influence of damping by the free stream flow and hinders the formation of and interaction with a leading-edge vortex. In the study mentioned above, Yeh *et al.* [26]
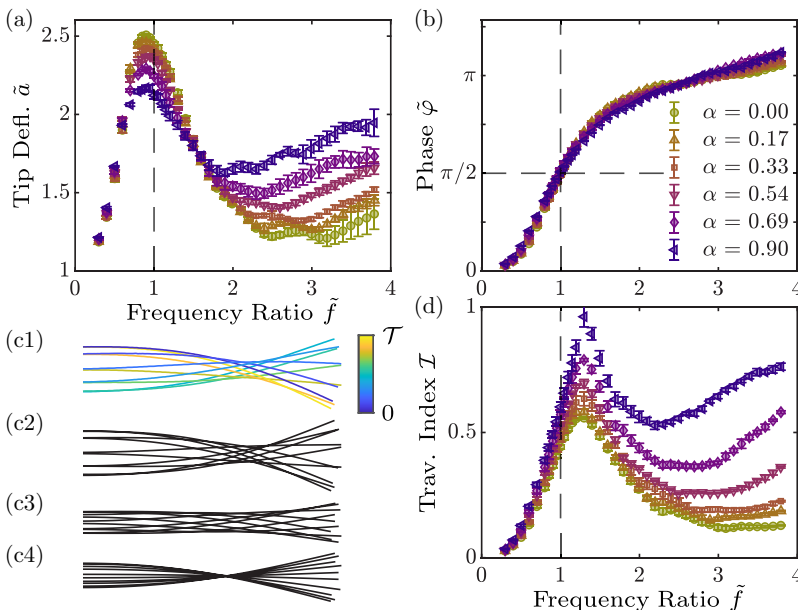
FIG. 4. Kinematics of the flapping foils. (a) Normalized tip deflection $\tilde{a}$ and (b) phase $\tilde{\varphi}$ of the tip relative to the root as functions of the frequency ratio $\tilde{f}$. (c) Snapshots of a deformed profile of the flapping foil with $\alpha = 0.54$ at $\tilde{f} = 2$. (c1) Measured center line and (c2) reconstruction from the first mode of complex orthogonal decomposition (COD) with its (c3) traveling and (c4) standing-wave components. (d) Traveling index $\mathcal{I}$ as a function of the frequency ratio $\tilde{f}$.

investigated both the fixed configuration (where the propulsor is constrained not to move as in our paper) and the free-swimming case (where the foil reaches a steady-state velocity). Whereas they observed similar results for both cases, we cannot ascertain, based on experimental evidence, the applicability of our findings for situations where a non-negligible background flow arises. Studying this alternative configuration would have required different and significantly more challenging experimental considerations, which go beyond the scope of the present paper. We hope that future investigations will continue addressing these questions in the presence of a background flow.

Another numerical study [30] considered foils with distributed stiffness in a 2D inviscid fluid, finding that concentrating the stiffness towards the root maximizes thrust production if no resonance can be triggered. This paper also speculates that, in the presence of drag, efficiency-maximizing distributions will tend to be thrust-maximizing ones, which is confirmed by our observations. Even though these inviscid results are not directly applicable to our system, the highlighted importance on the separate roles of the mean stiffness, and its distribution underlies our choice to fix $\langle B \rangle$ to perform a fair comparison across various foils with different stiffness distributions. To the best of our knowledge, our paper is the first experimental work in which independent control of $\langle B \rangle$ (or M) was achieved to accurately characterize the performance of flapping foils.

IV. KINEMATICS OF THE FLAPPING FOILS

We proceed to analyze the kinematics of the flapping foils with the goal of gaining further insight into the mechanism underlying the improvement of thrust and efficiency with tapering. The centerlines of the deformed foils during flapping were presented in Fig. 1(c) from which we can quantify the kinematics of the tip.

In Fig. 4(a), we plot the normalized maximum tip deflection $\tilde{a} = a/A_0$ of the iso-$\langle B \rangle$ flapping foils as a function of $\tilde{f}$. For all tapering ratios (α), the deflection reaches a maximum at $\tilde{f} \approx 0.9$

(slightly below resonance) with lower tip deflections for the more tapered samples. This trend is reversed for $\tilde{f} \gtrsim 1.55$ with higher $\tilde{a}$ for foils with higher values of α. By contrast, in Fig. 3(a), we saw that thrust increases monotonically with α. Even though higher tip deflections have previously been associated with higher thrust production [13,36], this is not compatible with our results. The phase lag $\tilde{\varphi}$ between the tip of a flapping foil and the root has also been claimed as a proxy for efficient flapping propulsion [15]. This statement is also not compatible with our results, at least, in the explored range of parameters as indicated by the results plotted in Fig. 4(b) that reveal an identical behavior for all samples. Overall, our experimental results indicate that neither the motion of the tip nor its phase with respect to the driving motion can alone be related to the increase in thrust with tapering.

Both the tip deflection and the phase are pointwise quantities that do not capture the global undulatory motion. Next, we assess whether our flapping foils exhibit traveling-wave kinematics, which is known to be highly efficient in flapping locomotion [37,38]. To do so, we perform a complex orthogonal decomposition (COD) [39] on the recorded deformation profiles. The COD is a generalization of proper orthogonal decomposition (POD) [40] and is especially suited to the analysis of wave kinematics [41]. The POD method gives the decomposition of a quantity [i.e., the deformed centerline, $Y(x,t)$ in our case] as a sum of orthogonal spatial modes u_j with their respective temporal coefficients b_j; $Y(x,t) \approx \sum_j b_j(t)u_j(x)$. Both u_j and b_j are complex numbers when extracted with the COD, given that the input for the algorithm is $Y_{\text{COD}} = Y + i\mathcal{H}(Y)$; the real part is the original data, and the imaginary part is its Hilbert transform. In our system, the first mode ($j = 1$) captures the main features of the deformation. By way of example, in Fig. 4(c1), we present representative snapshots of the deformation of the centerline ($\alpha = 0.54$ at $\tilde{f} = 2$), and in Fig. 4(c2), the equivalent reconstructed profiles obtained from $\text{Re}\{b_1 u_1\}$ (the real part of $b_1 u_1$). We find excellent agreement between the recorded centerline deformation [Fig. 4(c1)] and its one-mode-reconstruction [Fig. 4(c2)].

The COD method also enables the decomposition of the deformation profiles into a traveling wave component [Fig. 4(c3)] and a standing wave component [Fig. 4(c4)]. To distinguish between standing-wave-dominated and traveling-wave-dominated kinematics in a complex mode u_j, one can use a *traveling index* [39] $\mathcal{I}$, defined as the inverse of the condition number of $[\text{Re}\{u_j\}, \text{Im}\{u_j\}]$; i.e., the matrix whose two columns are the real and imaginary part of the mode u_j. A pure traveling-wave regime yields $\mathcal{I} = 1$ (since $\text{Re}\{u_j\}$ and $\text{Im}\{u_j\}$ are orthogonal and of the same magnitude), whereas $\mathcal{I} = 0$ for a a standing-wave-like regime (i.e., a mode with its two components parallel or of differing magnitudes).

In Fig. 4(d), we plot the traveling index $\mathcal{I}$ of the first mode of COD for each iso-$\langle B \rangle$ foil as a function of $\tilde{f}$ for different tapering ratios. Over the entire frequency range, samples with higher values of α (more tapered) yield increasing values of $\mathcal{I}$. This traveling index orders the curves for different values of α in the same way observed for both the thrust and the efficiency curves (Fig. 3). Consequently, we find that $\mathcal{I}$ holds a stronger connection to the propulsive performance discussed above than the tip deflection. The relationship between the dynamic performance and the kinematics is further discussed in the Supplemental Material [35] where we present $C_P(\mathcal{I})$ and $\varepsilon(\mathcal{I})$ curves for different values of α. Increasing the tapering of a foil promotes the occurrence of a traveling wave during flapping, an effect that we speculate is at the core of the observed increase in efficiency.

V. FLOW FIELD GENERATED BY THE FLAPPING FOILS

Thus far, we have focused on the elastodynamics of flapping foils without studying the fluid explicitly. Next, we investigate the flow field in the neighborhood of the foil's tip with an emphasis on quantifying how the tapering of the foils affects the topology and strength of the vortices shed in their wake.

We used PIV to measure the flow field using 56-μm polyamid seeding particles (Vestosint 2157, Evonik). The PIV imaging system was composed of a light-emitting diode pulsing system (LPS3, ILA_5150 GmbH) to generate a light sheet at midwidth of the foils, parallel to the fluid surface,
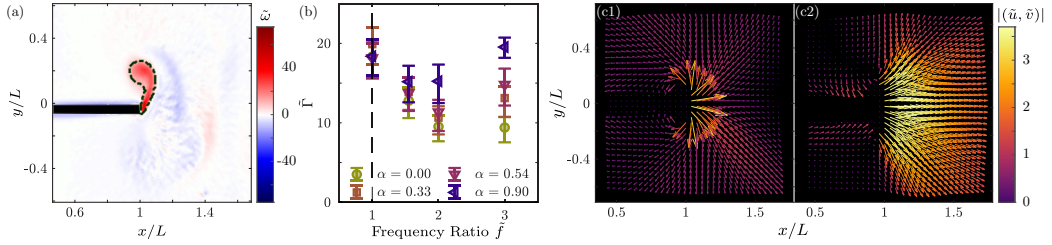
FIG. 5. PIV results and derived vorticity and circulation measures. (a) Snapshots of the nondimensional vorticity $\tilde{\omega}$, phase averaged over one stroke ($\alpha = 0.54$, $\tilde{f} = 1.55$). The boundary S used to compute the circulation Γ is shown as a dashed line. (b) Mean circulation $\tilde{\Gamma}$ versus $\tilde{f}$. The error bars correspond to a threshold value $\pm 20\%$ above/below $\tilde{\omega}_t = 10$, demonstrating that the observed trends are weakly dependent on this choice. (c) Mean velocity flow at $\tilde{f} = 3$ for (c1) the flat flapping foil ($\alpha = 0$) and (c2) the most tapered one ($\alpha = 0.90$) [see Fig. 1(d) for the corresponding kinematics]. The scale of the arrows size is different in the two plots, whereas their actual magnitude $|(\tilde{u}, \tilde{v})|$ is encoded in the adjacent color map.

and a complementary metal-oxide semiconductor camera (2048×2048 px, UI-3370SE-M-GL, IDS Imaging Development Systems GmbH) connected to a timing unit (Synchronizer, ILA_5150 GmbH). The camera's field of view was zoomed in to the tip of the flapping foil and its near wake. The velocity and vorticity fields were obtained using the software PIVVIEW (v3.9, PIVTEC GmbH). The experimental images were processed using a multigrid algorithm with a resulting interrogation window size of 48×48 px and a 66% overlap, leading to a resolution of 0.92 mm ($\approx 0.01L$) for the spacing between the velocity vectors. We focused on a representative selection of the iso-$\langle B \rangle$ flapping foils ($\alpha = 0$, 0.33, 0.54, and 0.90) at four values of the frequency ratio $\tilde{f} = 1, 1.55, 2,$ and 3.

In Fig. 5(a), we show a representative snapshot of the nondimensionalized vorticity ($\tilde{\omega} = \omega / f$) during the stroke of a flapping foil with moderate tapering ($\alpha = 0.54$). We see a positive vortex (red regions) generated at the tip, as well as the previous negative vortex (blue regions) dissipating downstream (corresponding video available in the Supplemental Material [35]); a wake structure known as reverse von Kármán street that is characteristic of fish swimming [42,43]. This pattern of vortices, generated at the tip and shed on each stroke, was common for all the foils and frequencies that we explored.

The relative strength of the generated vortices depended on both α and $\tilde{f}$. To quantify these variations, we computed the circulation $\Gamma = \int_S \omega \, dS$ of the main coherent concentrations of vorticity. Here, S is the boundary of the integration surface set by a threshold value $\tilde{\omega}_t = 10$, chosen to isolate the created vortex and its connected shear layer [see dashed curve in Fig. 5(a)]. For both negative and positive vorticities, we compute the period average of the circulation $\Gamma^{\pm} = \int_{S(\pm \tilde{\omega}_t)} \omega \, dS$. As a measure for the overall vortex strength, we take the respective mean circulations $|\overline{\Gamma}^+|$ and $|\overline{\Gamma}^-|$ and scale them as $\tilde{\Gamma} = (|\overline{\Gamma}^+| + |\overline{\Gamma}^-|)/(2faL)$, where fa corresponds to the characteristic maximum tip velocity. In Fig. 5(b), we plot $\tilde{\Gamma}$ versus $\tilde{f}$, finding that the more tapered foils generate stronger vortices. Consistently, we find that the circulation increases with α. This finding is particularly interesting for the case with $\tilde{f} = 1.55$ since all flapping foils have the same tip deflection [see Fig. 4(a)].

Finally, we focus on the structure of the wake. In Fig. 5(c), we present two period-averaged velocity fields, $(\tilde{u}, \tilde{v}) = (u/fa, v/fa)$ at $\tilde{f} = 3$ for the extreme cases of the flat ($\alpha = 0$) and the most tapered ($\alpha = 0.90$) foils. The flat specimen emanates an almost radial flow from its tip. The fluid that is not directed downstream does not contribute to the propulsive force, thereby leading to a loss in thrust. By contrast, the most tapered foil expels the surrounding fluid mostly downstream. For intermediate values of α, the mean wake features two symmetric jets angled downstream, similar to passive pitching panels [44]. These results indicate that the mean wake patterns that we have

observed are directly related to the kinematics discussed above with traveling-wave kinematics enhancing the downstream fluid flow and enhancing thrust.

VI. DISCUSSION AND CONCLUSION

The present experimental paper demonstrates that concentrating the stiffness towards the root of flapping propulsors significantly enhances both thrust production and efficiency over a wide range of driving frequencies, at least, in the range of parameters that we considered.

Many biological systems, such as fish deform actively to produce efficient undulatory motions; distributing the stiffness has a similar outcome in our tapered flapping foils, which are purely passive. In the absence of distributed actuation, tuning the stiffness profile serves as a means to enhance the traveling-wave kinematics, thereby impacting the resulting wake and the characteristics of propulsion.

This mechanism appears to be robust as evidenced by the similar behavior observed for the iso-$\langle B \rangle$ and iso-M sets of foils. We hope that our thorough experimental analysis will instigate future theoretical and computational work toward further formalizing the underlying mechanism relating tapering, thrust, and efficiency of flapping foils. Ultimately, such developments could serve as a rational ground for the design optimization of efficient flapping propulsion systems and small underwater vehicles.

[1] W. Shyy, H. Aono, S. K. Chimakurthi, P. Trizila, C. Kang, C. E. S. Cesnik, and H. Liu, Recent progress in flapping wing aerodynamics and aeroelasticity, Prog. Aerosp. Sci. **46**, 284 (2010).

[2] A. J. Smits, Undulatory and oscillatory swimming, J. Fluid Mech. **874**, P1 (2019).

[3] K. N. Lucas, N. Johnson, W. T. Beaulieu, E. Cathcart, G. Tirrell, S. P. Colin, B. J. Gemmell, J. O. Dabiri, and J. H. Costello, Bending rules for animal propulsion, Nat. Commun. **5**, 3293 (2014).

[4] G. V. Lauder and P. G. A. Madden, Fish locomotion: kinematics and hydrodynamics of flexible foil-like fins, Exp. Fluids **43**, 641 (2007).

[5] S. A. Combes and T. L. Daniel, Flexural stiffness in insect wings i. scaling and the influence of wing venation, J. Exp. Biol. **206**, 2979 (2003).

[6] S. Alben, Optimal flexibility of a flapping appendage in an inviscid fluid, J. Fluid Mech. **614**, 355 (2008).

[7] S. Michelin and S. G. L. Smith, Resonance and propulsion performance of a heaving flexible wing, Phys. Fluids **21**, 071902 (2009).

[8] S. Alben, C. Witt, T. V. Baker, E. Anderson, and G. V. Lauder, Dynamics of freely swimming flexible foils, Phys. Fluids **24**, 051901 (2012).

[9] F. Paraz, L. Schouveiler, and C. Eloy, Thrust generation by a heaving flexible foil: Resonance, nonlinearities, and optimality, Phys. Fluids **28**, 011903 (2016).

[10] M. Piñeirua, B. Thiria, and R. Godoy-Diana, Modelling of an actuated elastic swimmer, J. Fluid Mech. **829**, 731 (2017).

[11] Q. Zhu, Numerical simulation of a flapping foil with chordwise or spanwise flexibility, AIAA J. **45**, 2448 (2007).

[12] M. Vanella, T. Fitzgerald, S. Preidikman, E. Balaras, and B. Balachandran, Influence of flexibility on the aerodynamic performance of a hovering wing, J. Exp. Biol. **212**, 95 (2009).

[13] P. D. Yeh and A. Alexeev, Free swimming of an elastic plate plunging at low reynolds number, Phys. Fluids **26**, 053604 (2014).

[14] Y. Zhang, C. Zhou, and H. Luo, Effect of mass ratio on thrust production of an elastic panel pitching or heaving near resonance, J. Fluids Struct. **74**, 385 (2017).

[15] S. Ramananarivo, R. Godoy-Diana, and B. Thiria, Rather than resonance, flapping wing flyers may play on aerodynamics to improve performance, Proc. Natl. Acad. Sci. USA **108**, 5964 (2011).

[16] P. A. Dewey, B. M. Boschitsch, K. W. Moored, H. A. Stone, and A. J. Smits, Scaling laws for the thrust production of flexible pitching panels, J. Fluid Mech. **732**, 29 (2013).

[17] D. B. Quinn, G. V. Lauder, and A. J. Smits, Scaling the propulsive performance of heaving flexible panels, J. Fluid Mech. **738**, 250 (2014).

[18] F. Ayancik, Q. Zhong, D. B. Quinn, A. Brandes, H. Bart-Smith, and K. W. Moored, Scaling laws for the propulsive performance of three-dimensional pitching propulsors, J. Fluid Mech. **871**, 1117 (2019).

[19] D. Floryan and C. W. Rowley, Clarifying the relationship between efficiency and resonance for flexible inertial swimmers, J. Fluid Mech. **853**, 271 (2018).

[20] A. Goza, D. Floryan, and C. Rowley, Connections between resonance and nonlinearity in swimming performance of a flexible heaving plate, J. Fluid Mech. **888**, A30 (2020).

[21] S. A. Combes and T. L. Daniel, Flexural stiffness in insect wings II. spatial distribution and dynamic wing bending, J. Exp. Biol. **206**, 2989 (2003).

[22] J. L. Tangorra, G. V. Lauder, I. W. Hunter, R. Mittal, P. G. A. Madden, and M. Bozkurttas, The effect of fin ray flexural rigidity on the propulsive forces generated by a biorobotic fish pectoral fin, J. Exp. Biol. **213**, 4043 (2010).

[23] P. Riggs, A. Bowyer, and J. Vincent, Advantages of a biomimetic stiffness profile in pitching flexible fin propulsion, J. Bionic. Eng. **7**, 113 (2010).

[24] K. Shoele and Q. Zhu, Performance of a wing with nonuniform flexibility in hovering flight, Phys. Fluids **25**, 041901 (2013).

[25] K. N. Lucas, P. J. M. Thornycroft, B. J. Gemmell, S. P. Colin, J. H. Costello, and G. V. Lauder, Effects of non-uniform stiffness on the swimming performance of a passively-flexing, fish-like foil model, Bioinspir. Biomim. **10**, 056019 (2015).

[26] P. D. Yeh, Y. Li, and A. Alexeev, Efficient swimming using flexible fins with tapered thickness, Phys. Rev. Fluids **2**, 102101(R) (2017).

[27] A. K. Kancharala and M. K. Philen, Optimal chordwise stiffness profiles of self-propelled flapping fins, Bioinspir. Biomim. **11**, 056016 (2016).

[28] W. Wang, H. Huang, and X.-Y. Lu, Optimal chordwise stiffness distribution for self-propelled heaving flexible plates, Phys. Fluids **32**, 111905 (2020).

[29] M. N. J. Moore, Torsional spring is the optimal flexibility arrangement for thrust production of a flapping wing, Phys. Fluids **27**, 091701 (2015).

[30] D. Floryan and C. W. Rowley, Distributed flexibility in inertial swimmers, J. Fluid Mech. **888**, A24 (2020).

[31] J. N. Lee, C. Park, and G. M. Whitesides, Solvent compatibility of poly(dimethylsiloxane)-based microfluidic devices, Anal. Chem. **75**, 6544 (2003).

[32] M. Pezzulla, E. F. Strong, F. Gallaire, and P. M. Reis, Deformation of porous flexible strip in low and moderate reynolds number flows, Phys. Rev. Fluids **5**, 084103 (2020).

[33] B. Audoly and Y. Pomeau, *Elasticity and Geometry* (Oxford University Press, Oxford, 2010).

[34] T. Van Buren, D. Floryan, N. Wei, and A. J. Smits, Flow speed has little impact on propulsive characteristics of oscillating foils, Phys. Rev. Fluids **3**, 013103 (2018).

[35] See Supplemental Material at https://link.aps.org/supplemental/10.1103/PhysRevFluids.7.074403 for discussions on the choice of performance coefficients (S.I) and on the relationship between the dynamics and kinematics of our flapping foils. A movie of the vorticity field, corresponding to Fig. 5(a), is also provided.

[36] M. Hultmark, M. Leftwich, and A. J. Smits, Flowfield measurements in the wake of a robotic lamprey, Exp. Fluids **43**, 683 (2007).

[37] T. Y.-T. Wu, Swimming of a waving plate, J. Fluid Mech. **10**, 321 (1961).

[38] M. J. Lighthill, Note on the swimming of slender fish, J. Fluid Mech. **9**, 305 (1960).

[39] B. F. Feeny, A complex orthogonal decomposition for wave motion analysis, J. Sound Vib. **310**, 77 (2008).

[40] K. Taira, S. L. Brunton, S. T. M. Dawson, C. W. Rowley, T. Colonius, B. J. McKeon, O. T. Schmidt, S. Gordeyev, V. Theofilis, and L. S. Ukeiley, Modal analysis of fluid flows: An overview, AIAA J. **55**, 4013 (2017).

[41] Z. Cui, Z. Yang, L. Shen, and H. Z. Jiang, Complex modal analysis of the movements of swimming fish propelled by body and/or caudal fin, Wave Motion **78**, 83 (2018).

[42] M. Sfakiotakis, D. M. Lane, and J. B. C. Davies, Review of fish swimming modes for aquatic locomotion, IEEE J. Oceanic Eng. **24**, 237 (1999).

[43] D. Floryan, T. Van Buren, and A. J. Smits, Swimmers' wake structures are not reliable indicators of swimming performance, Bioinspir. Biomim. **15**, 024001 (2020).

[44] H. Hu, J. Wang, Y. Wang, and H. Dong, Effects of tunable stiffness on the hydrodynamics and flow features of a passive pitching panel, J. Fluids Struct. **100**, 103175 (2021).